

Angle- and Delay-Dispersion Characteristics in a Hallway and Lobby at 60 GHz*

Ruoyu Sun¹, Peter B. Papazian¹, Jelena Senic¹, Camillo Gentile², Kate A. Remley¹

¹ RF Technology Division, National Institute of Standards and Technology, Boulder, CO, USA, ruoyu.sun@nist.gov

² Wireless Networks Division, National Institute of Standards and Technology, Gaithersburg, MD, USA

* Publication of the United States government, not subject to copyright in the U.S.

Abstract—In this paper, we present results from measurement data collected in a hallway and lobby up to 33 meters in line-of-sight and non-line-of-sight conditions. The data were collected with a custom double-directional 60 GHz channel sounder. By tracking the angle-of-departure and angle-of-arrival of the strongest path, regions with a direct path as well as single-, double- and triple-bounce paths are identified. This was validated against the geometry of the hallway. In addition, power angle- and delay- profiles are presented as well as complementary root-mean-square angle and delay spreads. The root-mean-square delay spread was characterized with variable beamwidth using a synthetic antenna pattern applied in post processing.

Index Terms—millimeter-wave wireless, multiple-input-multiple-output antenna array, phased-array antenna, propagation channel, measurement, wireless systems.

I. INTRODUCTION

Due to saturation of the sub-6 GHz bands over the past decade, the wireless industry is expanding to the millimeter-wave (mmWave) spectrum for 5G deployment (by definition 30 – 300 GHz). To compensate for the much higher path loss in this frequency regime, very high-gain phased-array antennas (in excess of 26 dBi) will likely be employed at both the transmitter (TX) and receiver (RX). The higher the gain, the narrower the beamwidth; pencilbeams arrays on the order of a few degrees beamwidth are currently under design [1]. Because their beamwidths are so small, the boresights of TX and RX antennas must be steered towards viable propagation paths between the respective TX and RX.

In line-of-sight (LOS) conditions, the beams will be steered towards the direct path, which is typically the strongest available. When obstructed – say by human bodies which severely attenuate the signal – the beams must be redirected towards other available paths to maintain connectivity. Even if the direct path is clear, other strong propagation paths are necessary to implement spatial multiplexing. Hence, knowing the angle spread, a key measure of the relative strength of the various paths, is important. In non-line-of-sight (NLOS) conditions, the direct path will likely go undetected altogether since materials have much higher penetration losses at mmWave frequencies [2]. Thus, in NLOS, understanding the spread of power in the various directions is even more critical.

The delay spread is also a very important quantity, the longer the spread, the more processing is required for equalization, thereby increasing the cost of hardware. Once a

suitable path has been found for beamforming, the pencilbeam antennas can hone in on the path, reducing the delay spread significantly by admitting fewer paths into the beam.

In this paper, we report on the root-mean-square angle spread (RMS-AS) and delay spread (RMS-DS) derived from measurements conducted in a lobby and hallway environment in both LOS and NLOS conditions. The measurements were taken using our custom double-directional channel sounder at 60.5 GHz [3]. The measurement campaign and details of the equipment are described in Section II, followed by a description of the dominant propagation mechanisms in the environment in Section III. Section IV presents our results and finally our conclusions are documented in the last section.

II. MEASUREMENTS

A. Measurement Equipment

Fig. 1(a) displays the TX and RX of our 60 GHz channel sounder. The TX features a semicircular array of eight horn antennas, each with 18.1 dBi gain and 22.5° beamwidth (identical in vertical and horizontal planes). To avoid any “blind spots,” the angular spacing between the elements matches the beamwidth of the horns. Specifically, the elements are spaced at 22.5° horizontally, and vertically adjacent elements are pointed outwards at 0° and upwards at 22.5°. Consequently, the horizontal beamwidth of the array is 180° and its vertical beamwidth is 45°. The 3D spatial diversity allows for characterizing the antennas angle-of-departure (AoD) in both azimuth and elevation. The RX features two semicircular arrays to estimate angle-of-arrival (AoA) – each one is a replica of the TX array – extending the azimuthal beamwidth of the array to an omnidirectional view. The omnidirectional design at the RX is essential because the RX is mounted on a mobile robotic positioning system, whereas the TX is fixed – typical for hot-spot deployments – hence emission from the backside of the TX is less important.

The transmitting system generates a repeating 2047-bit pseudorandom (PN) codeword that has a chip rate of 2 GHz, equivalent to a delay resolution of 0.5 ns, transmitted at 20 dBm. With precision synchronization using Rubidium clocks, the signal is transmitted from a single TX element while the received signal is measured by sequentially switching through the RX elements every two codewords. Note that the extra codeword is used to buffer the electronic switching time. After a full RX cycle, the TX element is then also switched to the next TX element. Thus, a measurement consisting of a full sweep of the 128 (8 × 16) pairs requires 262 μs. The codeword

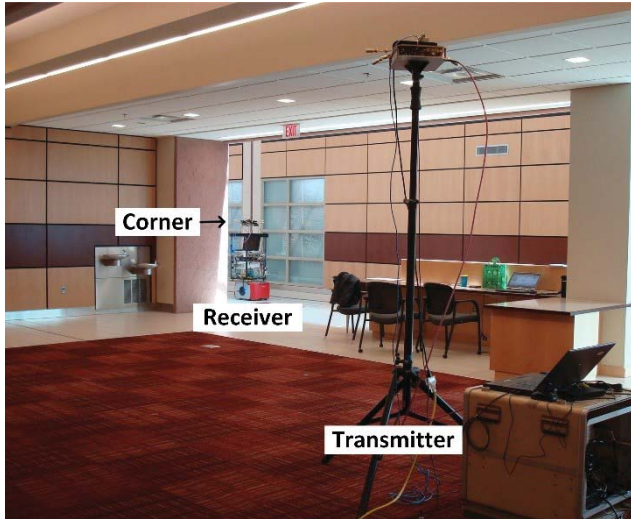


Fig. 1(a). Photo of the measurement system and the lobby site. The TX antenna array is mounted on a tripod and the RX antenna array is placed on the robotic mobile positioning system.

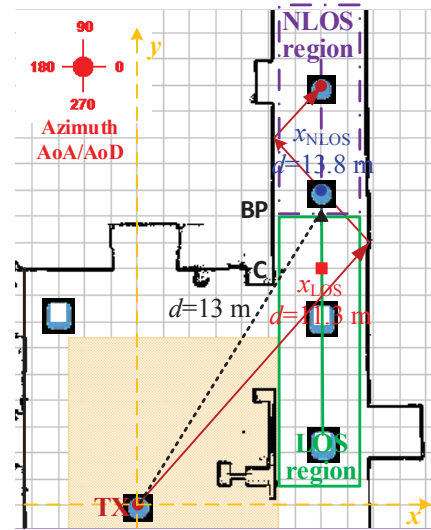


Fig. 1(b). Floorplan of the hallway/lobby. TX was placed in the lobby area and RX was moving along the hallway in LOS (solid green line) and NLOS (dash-dotted purple line) conditions. Raytracing prediction for the reflected path along the hallway is depicted with red solid arrows.

is generated at an intermediate frequency (IF) of 3 GHz and then upconverted to an RF center frequency of $f_c = 60.5$ GHz. At the RX, the received signal is downconverted back to the IF and then digitized at 40 G samples/sec. For each TX/RX measurement pair, the received signal is correlated with the known PN codeword to generate a complex channel impulse response (CIR). Non-ideal effects from the electronics within the TX and RX are carefully corrected with back-to-back measurements [3]. The dynamic range of the sounder is 162.2 dB [3].

B. Measurement Campaign

Measurements were performed in a hallway/lobby inside the Physical Measurement Laboratory (PML) building on the National Institute of Standards and Technology (NIST) campus in Boulder, CO USA. The height of the ceiling is 3 m in the lobby and 7 m in the hallway. The width of the hallway is approximately 4 m. The walls are made of finely ribbed wood, glass (with flat surface) or concrete with a rough, stone-like surface. The floor is covered with carpet in the lobby area and porcelain tiles in the hallway. The ceiling is made of acoustic tiles. Occasionally people were walking in the area.

To emulate a hot-spot deployment, the TX was fixed in the lobby area at 2.5 m height while the RX was mounted on the mobile-positioning robot 1.6 m above the floor. Fig. 1(a) shows a snapshot of the deployment with the TX positioned in the lobby area and the RX moving in the hallway close to a corner. The TX was oriented to cover the continuous azimuth-angle ranges from 320° to 140° (defined in Fig. 1(b)) so that most of the energy was transmitted towards the hallway direction.

A floorplan of the environment marked with the TX position and the RX trajectory along the hallway is shown in Fig. 1(b). The map, with a grid spacing of 1 m, was created with the robot's laser range-finder. The x and y axes and the

orientation of the azimuth angle are also marked. The robot moved along a straight line in the middle of the hallway at a constant velocity of 0.08 m/s. The corresponding TX-RX distance d ranged from 7.5 m to 33.5 m. Note that, due to inconstant data-writing speed from the buffer on the digitizer to the solid-state hard drive, data for distances $25.2 \text{ m} < d < 29.2 \text{ m}$ were not recorded. The robot transitioned from LOS (green solid line) to NLOS (dash-dotted purple line) conditions after the breakpoint (BP) right after the corner (C). The NLOS conditions were created by the interfering walls. The robot's mobile positioning system reports its position, velocity and heading at each data collection point. We collected 365 omnidirectional power-angle-delay profiles (PADPs).

III. DATA ANALYSIS

In post-processing, the 128 CIRs from a single measurement were combined through the space-alternating generalized expectation-maximization (SAGE) algorithm [4] in order to extract the channel multipath components (MPCs). Given the phase centers of the TX and RX horns gauged within an accuracy of $50 \mu\text{m}$ [3], the departure and arrival angles were estimated by comparing the arrival times of the MPCs between the various CIRs. The accuracy of the angle estimation for the direct path was estimated with an average error of 2.1° [3]. Upon extraction, the path gain (PG_i) of the i^{th} MPC is indexed according to delay (τ_i), departure angle at the TX ($\theta_i^{TX}, \phi_i^{TX}$), and arrival angle at the RX ($\theta_i^{RX}, \phi_i^{RX}$), where θ denotes azimuth and ϕ elevation. The SAGE algorithm also de-embeds the directional antenna patterns of the array elements, estimated from the manufacturer's specifications. In this section, we analyze the MPCs to describe the propagation mechanisms in play throughout the lobby/hallway environment.

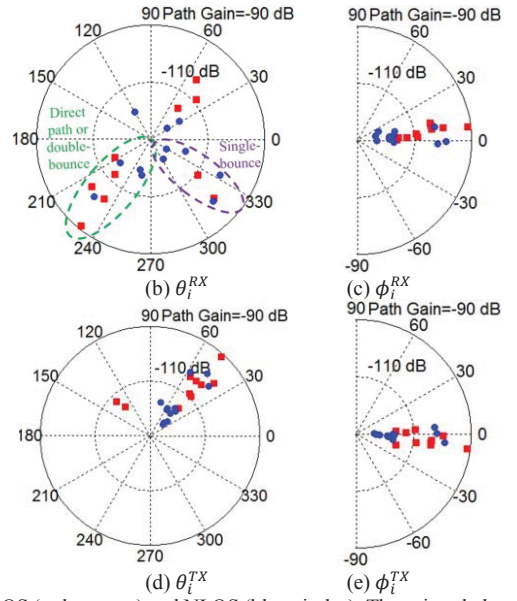
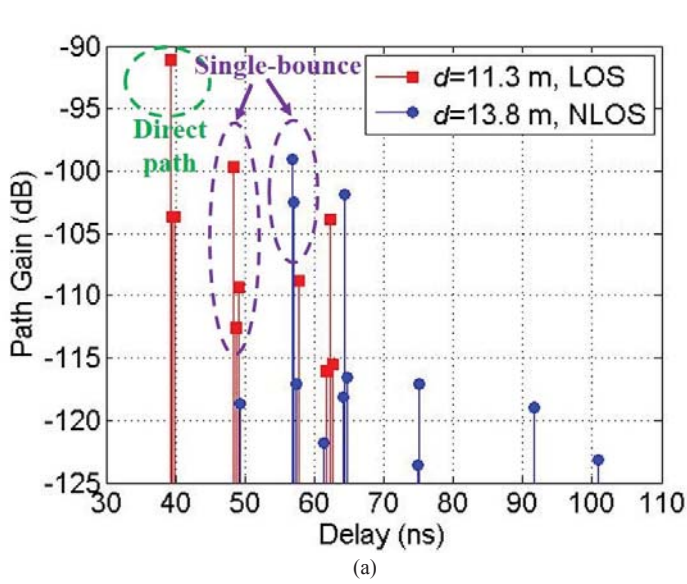


Fig. 2 Power-delay profiles (a) and power-angle profiles (b)-(e) for two example locations in LOS (red squares) and NLOS (blue circles). The azimuthal power-angle profile is shown in (b) and (d) over 360° , while the elevation is shown in (c) and (e) over 180° only.

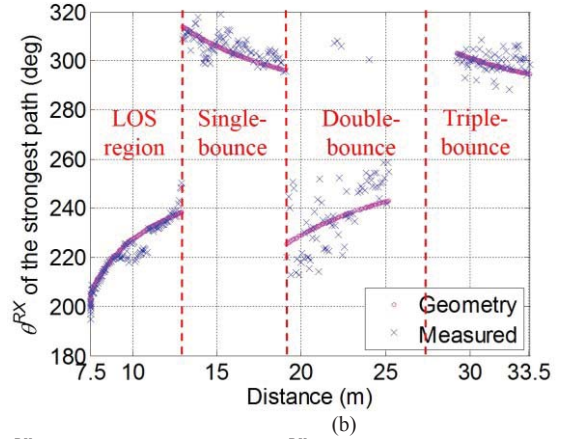
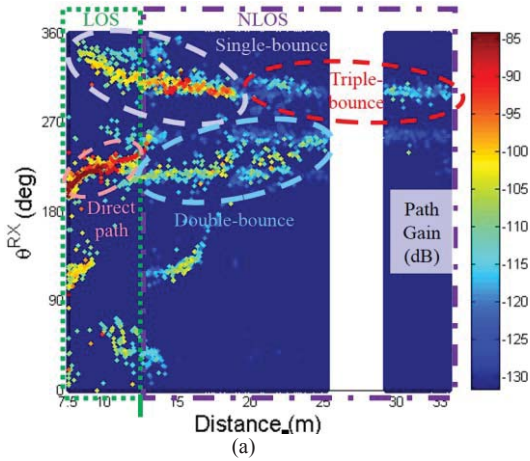


Fig. 3. PAPs for all measurement locations, (a) Sequence of PAPs over distance for θ^{RX} , (b) Azimuth arrival angle (θ^{RX}) of strongest path over distance.

A. Illustrative Example with Two Locations

We first consider an illustrative example at two specific measurement locations. One location was in LOS conditions right before the breakpoint (\mathbf{x}_{LOS} at $d = 11.3$ m) and the other in NLOS right after the breakpoint (\mathbf{x}_{NLOS} at $d = 13.8$ m). The locations are marked in Fig. 1(b).

The path gain of the MPCs versus delay, often referred to as the *power-delay profile* (PDP), for the two locations are superimposed in Fig. 2(a). For \mathbf{x}_{LOS} , the three paths clustered at $\tau_i = 39.3, 39.4$ and 39.9 ns represent the direct path – the strongest of the three – followed by the weaker reflections off of the wall near the corner. Note that when the robot moves up the hallway into an NLOS condition at \mathbf{x}_{NLOS} , the direct path is no longer detected, as mmWave signals cannot penetrate these materials; rather, they are replaced by the much weaker single path at 49.2 ns representing diffraction from the corner [2]. The second cluster of paths for \mathbf{x}_{LOS} and \mathbf{x}_{NLOS} together represent the paths reflected from the right

wall in the hallway. The path for \mathbf{x}_{LOS} at 48.4 ns represents the specular component followed by two weaker diffuse components at 48.7 and 49.1 ns. Analogously, the strongest path for \mathbf{x}_{NLOS} at 56.7 ns represents the specular component followed by two weaker diffuse components at 57.1 and 57.5 ns. The later paths in the PDPs represent reflections from other walls or obstacles in the environment or permutations thereof.

Analogously, Figs. 2(b)-(e) display the path gain of the MPCs versus each of the four angles, often referred to as the *power-angle profile* (PAP), for the two locations. Note the angles of the direct path for \mathbf{x}_{LOS} – the strongest path with $PG_i = -92$ dB: its elevation departure and arrival angles are slightly negative (-5°) and positive (6°), as expected, given that the TX is higher than the receiver. In fact, most arrivals follow the same trend for \mathbf{x}_{LOS} – and \mathbf{x}_{NLOS} too – barring exceptions for the ground bounces. The azimuthal AoD for both points are bound by the angles formed between the TX and the entrance to the hallway on the left and right sides, as energy can only propagate in the hallway since the interfering

walls are impenetrable by the signal. For the azimuthal AoA, the two clusters from Fig. 2(a) distinctly appear and are so labeled. All of the extracted angles agree with the geometry in the hallway/lobby area shown in Fig. 1(b).

B. All Locations Combined

The propagation mechanisms illustrated from the two example locations existed to some degree throughout all locations recorded in the lobby/hallway environment. Fig. 3(a) plots the power-angle profiles for the azimuthal arrival angle as a function of distance, where the clusters of MPCs of direct path, single-, double, triple-bounce and other scattering paths could be identified. Fig. 3(b) shows the azimuthal AoA of the strongest path as a function of distance. The theoretical results based on geometry is also provided in Fig. 3(b). Besides highlighting the direct path and single-bounce from the right wall of the hallway, as in the illustrative example in the last section, the plot shows the double-bounce from the right-then-left walls and the triple-bounce from the right-then-left-then-right walls. The θ^{RX} of the strongest path varies over 40° in the double-bounce region, while it only varies within 24° in the single- and triple-bounce regions. This is likely because the left wall is made of simulated rock, presenting a rough surface that scatters the signal over a larger range than the wooden wall with the finely ribbed surface on the right side of the hallway.

IV. ANGLE AND DELAY DISPERSION

The RMS-AS and RMS-DS are the most widely used measures for angle and delay dispersion, respectively. In this section, we compute their values for each of the measurements from the extracted MPCs. As the distance between the TX and RX increased, fewer and fewer MPCs were detected because they fell below the noise floor of the channel sounder, biasing the results towards smaller spreads. To avoid this, following common practice, we verified that the strongest MPC was at least 25 dB above the noise floor for each measurement in order for the measurement to be included in the results. The maximum distance observed that satisfied this condition was 18.9 m, which is the transition distance from the single-bounce region to double-bounce region. In addition, for each measurement we applied a 25 dB threshold from the strongest MPC so that spreads across all measurements were computed with the same dynamic range across. This resulted in a total of N remaining MPCs per measurement.

A. RMS Angle Spread

Since we extracted four different angles for each MPC, the angle spread was computed separately for $\varphi = \{\theta^{TX}, \phi^{TX}, \theta^{RX}, \phi^{RX}\}$. Specifically, the RMS-AS for each measurement was computed as

$$\sigma_\varphi = \sqrt{\frac{\sum_{i=1}^N P G_i \cdot (\varphi_i - \mu_\varphi)^2}{\sum_{i=1}^N P G_i}}, \quad (1)$$

$$\mu_\varphi = \frac{\sum_{i=1}^N P G_i \cdot \varphi_i}{\sum_{i=1}^N P G_i}, \quad (2)$$

where φ_i is the angle for the i^{th} MPC. We saw little variation in the departure and arrival elevation angles, ϕ^{TX} and ϕ^{RX} , in our measurements, primarily because the vertical distance between the TX and RX was much smaller than the horizontal distance. In fact, $\sigma_{\phi^{TX}}$ was observed only up to 11.2° with a median value of 2.8° ; similarly, $\sigma_{\phi^{RX}}$ was only up to 9.8° with a median value of 2.7° . While more variation was observed in the departure azimuth angle, θ^{TX} , since all of the detected energy in NLOS was channeled along the corridor, θ^{TX} only varied between the values corresponding to the left and right walls at the entrance to the hallway. Accordingly, $\sigma_{\theta^{TX}}$ was up to 43.7° with a median value of 3.7° .

By far the most variation was in the azimuthal arrival angle, θ^{RX} , because the RX array is omnidirectional in azimuth; also because, since the RX was in the hallway, paths could arrive from any azimuthal direction. In fact, θ^{RX} was up to 84.2° with a median value of 24.6° . Fig. 4(a) also presents $\sigma_{\theta^{RX}}$ as a function of distance. In LOS conditions, the figure shows that most of the detected energy was in the direct path but gave way to paths from other arrival directions as it weakened with increasing distance. Due to the absence of the direct path in NLOS, the energy was spread in multiple arrival directions, increasing the RMS-AS. The θ^{RX} RMS-AS was typically smaller than 60° but occasionally jumped to over 80° due to intermittent MPCs from smaller ambient objects. For example, the spike near 15 m was due to the cluster of MPCs shown in Fig. 3(a) at that same distance and for θ^{RX} between 110° and 150° .

B. RMS Delay Spread

Millimeter-wave systems will employ steerable pencilbeam antennas with beamwidths as low as 3° but unlikely greater than 30° [1]. As noted earlier, a larger angle spread means that more paths are available to steer energy from the directional TX to the directional RX. Smaller beamwidths will translate into narrower delay spreads as fewer paths will be admitted into the beam. Understanding this effect can help improve the design of pencilbeam antenna arrays.

In order to investigate this, we computed the RMS-DS by applying, after the MPCs have been extracted, an ideal, synthetic antenna pattern with variable beamwidth to the TX and RX. We assume a Gaussian beam pattern steered at $(\bar{\theta}, \bar{\phi})$ which can be expressed as

$$G^\omega(\theta, \phi; \bar{\theta}, \bar{\phi}) = e^{-\frac{(\theta - \bar{\theta})^2 + (\phi - \bar{\phi})^2}{\omega^2 / \log e^{16}}}, \quad (3)$$

where ω is the synthetic beamwidth of the antenna in both azimuth and elevation. At the TX, the beam is steered towards $(\bar{\theta}^{TX}, \bar{\phi}^{TX})$ and at the RX towards $(\bar{\theta}^{RX}, \bar{\phi}^{RX})$, corresponding to the respective departure angle and arrival angle of the strongest MPC in the measurement.

Fig. 3(b) shows $\bar{\theta}^{RX}$ versus distance for all measurements. Again, the reason we chose to illustrate $\bar{\theta}^{RX}$ is because the azimuthal arrival angle exhibits the most variability of the four

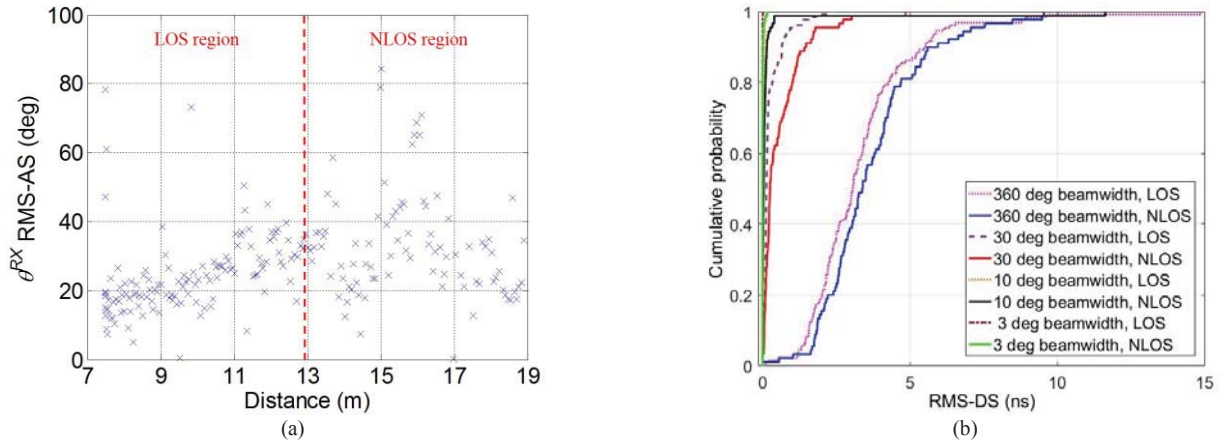


Fig. 4. Delay and angle spreads for all measurements, (a) RMS-AS of θ^{RX} over distance for measurements made in the hallway, (b) CDF of RMS-DS for various beamwidths synthetically applied in post processing at both TX and RX antennas for all measured data in the lobby/hallway scenario.

and, hence, may have the most significant impact on array design. The figure shows that in LOS conditions the strongest path is the direct path, while in NLOS conditions the receive array should be steered towards the single, second, and/or third wall bounces as the receiver advances up the hall. Note that the azimuthal AoA agrees with the geometry of the TX and RX locations with respect to the left and right walls.

By using the synthetic TX and RX beams, the directional delay spread was computed as

$$\sigma_{\tau}^{\omega} = \sqrt{\frac{\sum_{i=1}^N \bar{P}G_i^{\omega} \cdot (\tau_i - \mu_{\tau}^{\omega})^2}{\sum_{i=1}^N \bar{P}G_i^{\omega}}}, \quad (4)$$

$$\mu_{\tau}^{\omega} = \frac{\sum_{i=1}^N \bar{P}G_i^{\omega} \cdot \tau_i}{\sum_{i=1}^N \bar{P}G_i^{\omega}}, \quad (5)$$

where $\bar{P}G_i^{\omega} = PG_i \cdot G^{\omega}(\theta_i^{TX}, \phi_i^{TX}; \bar{\theta}^{TX}, \bar{\phi}^{TX}) \cdot G^{\omega}(\theta_i^{RX}, \phi_i^{RX}; \bar{\theta}^{RX}, \bar{\phi}^{RX})$ is the weighted path gain of the i^{th} MPC, all in linear scale.

In contrast to Fig. 4(a), no obvious trend was observed with distance for the RMS-DS. As such, Fig. 4(b) shows the cumulative distribution function (CDF) of the RMS-DS for the four beamwidths investigated in LOS and NLOS conditions. The RMS-DS in the NLOS region was slightly larger than in the LOS region, increasing with synthetic beamwidth. The maximum value of the RMS-DS for synthesized RX beamwidths of 3°, 10°, 30° and 360° are 0.2, 11.6, 4.9 and 14.9 ns, respectively. The median value was 3.1 ns for the 360° synthetic beamwidth and smaller than 0.2 ns for the other three synthetic beamwidths. These values agree well with those in [5], where the authors employed omnidirectional antennas at 60 GHz, and the RMS-DS in small offices, conference rooms, library and laboratory environments had a maximum value of 20 ns and a median value of approximately 3 to 6 ns, based on 20 or 30 dB multipath threshold, respectively [6].

V. CONCLUSION

We analyzed 60 GHz channel measurement data in a hallway/lobby scenario under both LOS and NLOS conditions. We included examples of individual power-delay

profiles and power-angle profiles. The channel evolution is illustrated by power-angle profiles over distance. The θ^{RX} of the strongest MPC clearly tracks LOS, single-, double- or triple-bounce regions, which agree with the geometry. We observed the rough wall surface strongly affects the TX RX antenna boresight direction in beamforming deployment. The θ^{RX} of the strongest MPC varied over a large range of over 40° when reflected from a rough wall surface, while the variation was less than 24° with reflection from a finely ribbed wooden wall. The RMS-AS is investigated that provides evidence for optimizing the beamwidth of antenna or antenna array in future 5G system design. The RMS-AS for θ^{RX} has a maximum value of 84.2° and the median value was 24.6°. The RMS-DS is studied with multiple synthetic beamwidths of 360°, 30°, 10° and 3°. The RMS-DS generally increases with synthesized beamwidth, but no strong trend with respect to distance is observed. Future work includes analysis for larger data sets, comparison of results over 28, 60 and 83 GHz.

REFERENCES

- [1] S. Zahir, O.D. Gurbuz, et. al. "60-GHz 64- and 256-Elements Wafer-Scale Phased-Array Transmitters Using Full-Reticle and Subreticle Stitching Techniques," *IEEE Transactions on Microwave Theory and Techniques*, vol. 64, no. 12, pp. 4701–4719, Nov. 2016.
- [2] J. Senic; C. Gentile; P. B. Papazian; K. A. Remley; J. K. Choi, "Analysis of E-band Path Loss and Propagation Mechanisms in the Indoor Environment," in *IEEE Transactions on Antennas and Propagation*, Early View, July 2017.
- [3] R. Sun, P. B. Papazian, J. Senic, Y. Lo, J. Choi, K. A. Remley, C. Gentile, "Design and Calibration of a Double-directional 60 GHz Channel Sounder for Multipath Component Tracking," *11th European Conference on Antennas and Propagation (EuCAP 2017)*, pp. 3336-3340, Paris, France, 19-24 Mar. 2017.
- [4] J. A. Fessler and A. O. Hero, "Space-alternating generalized expectation-maximization algorithm," *IEEE Transactions on Signal Processing*, vol. 42, no. 10, pp. 2664-2677, Oct. 1994.
- [5] T. Zwick, T. J. Beukema and Haewoon Nam, "Wideband channel sounder with measurements and model for the 60 GHz indoor radio channel," in *IEEE Transactions on Vehicular Technology*, vol. 54, no. 4, pp. 1266-1277, July 2005.
- [6] G. R. Maccartney, T. S. Rappaport, S. Sun and S. Deng, "Indoor Office Wideband Millimeter-Wave Propagation Measurements and Channel Models at 28 and 73 GHz for Ultra-Dense 5G Wireless Networks," in *IEEE Access*, vol. 3, pp. 2388-2424, 2015.